Metal–Organic Frameworks

International Edition: DOI: 10.1002/anie.201803262
German Edition: DOI: 10.1002/ange.201803262

From Metal–Organic Frameworks to Single-Atom Fe Implanted N-doped Porous Carbons: Efficient Oxygen Reduction in Both Alkaline and Acidic Media

*Long Jiao[+], Gang Wan[+], Rui Zhang, Hua Zhou, Shu-Hong Yu, and Hai-Long Jiang**

Abstract: *It remains highly desired but a great challenge to achieve atomically dispersed metals in high loadings for efficient catalysis. Now porphyrinic metal–organic frameworks (MOFs) have been synthesized based on a novel mixed-ligand strategy to afford high-content (1.76 wt %) single-atom (SA) iron-implanted N-doped porous carbon (Fe_{SA}-N-C) via pyrolysis. Thanks to the single-atom Fe sites, hierarchical pores, oriented mesochannels and high conductivity, the optimized Fe_{SA}-N-C exhibits excellent oxygen reduction activity and stability, surpassing almost all non-noble-metal catalysts and state-of-the-art Pt/C, in both alkaline and more challenging acidic media. More far-reaching, this MOF-based mixed-ligand strategy opens a novel avenue to the precise fabrication of efficient single-atom catalysts.*

Single-atom catalysts (SACs), a new research frontier in heterogeneous catalysis, have been intensively investigated in diverse reactions, including electrocatalysis, photocatalysis, and organic catalysis.[1–4] Given that only the coordinatively unsaturated metal atoms on the surface of solid catalysts contribute to the catalytic process, SACs would realize the utmost utilization of metal sites and thus greatly benefit the catalytic efficiency.[2] Furthermore, SACs are able to overcome the complicated multiple components in traditional supported metal catalysts and are regarded as ideal model catalysts to identify active sites and understand reaction process at a molecular level.[2,3] Though great progress has been achieved, the rational fabrication of SACs with high metal loadings (> 1 wt %) remains a grand challenge.[4] Along with the introduction of more active metals, the optimized pore structure, large surface area, and excellent conductivity in SACs, which would facilitate mass/electron transfer, are also desirable to improve the activity.[5]

To meet these challenges, metal–organic frameworks (MOFs),[6] a class of crystalline porous materials constructed by metal ions/clusters and versatile organic linkers, are promising candidates. MOFs have been demonstrated to be great precursors/templates to produce porous carbon-based materials via pyrolysis.[7,8] More importantly, their periodic structures give rise to spatial separation of building units and thus inhibit potential agglomeration of metal sites during pyrolysis, enabling MOFs ideal precursors to create SACs. Currently, the reports on MOF-pyrolyzed materials are mostly focused on the regulation of their pore features and compositions.[7d–g,8] The precise fabrication of active sites at the molecular level based on MOF precursors has been rarely reported. Very recently, zeolitic imidazolate frameworks (ZIFs) were reported as precursors to produce SACs based on structural tailorability, high nitrogen content, and the pore confinement effect.[4b,9] Unfortunately, the microporous feature of ZIFs and their derivatives hamper mass transfer and the accessibility of the active site.[9b] Therefore, it is imperative to develop SACs (providing efficient active sites) with hierarchical pores (benefitting mass transfer and active site accessibility) via the rational design of MOFs for improved catalytic performance.

With the above in mind, a porphyrinic MOF, PCN-222 (also called MOF-545 or MMPF-6),[10] featuring 1D mesochannels with a diameter of 3.2 nm (Supporting Information, Scheme S1), was chosen as a representative precursor. The ratio modulation between Fe-TCPP (TCPP = tetrakis (4-carboxyphenyl)porphyrin) and H_2-TCPP mixed ligands affords a series of isostructural MOFs, denoted as Fe_x-PCN-222 (x %: molar percentage of Fe-TCPP in both ligands) (Supporting Information, Scheme S2). The assembly of Fe-TCPP into 3D networks of Fe_x-PCN-222 effectively inhibits the molecular stacking, and the mixed-ligand strategy further expands the distance of adjacent Fe-TCPP ligands. Upon pyrolysis, the optimized Fe_{20}-PCN-222 can be converted into single-atom (SA) Fe sites implanted porous N-doped carbon, denoted as Fe_{SA}-N-C, with the unique mesopore character (Scheme 1). By integrating single Fe atoms (highly active sites) and hierarchically porous structure with oriented mesopores (facilitating active site access and mass transfer), the optimized Fe_{SA}-N-C exhibits superb oxygen reduction activity and ultrahigh stability, surpassing almost all reported

[*] L. Jiao,[+] R. Zhang, Prof. Dr. S.-H. Yu, Prof. Dr. H.-L. Jiang
Hefei National Laboratory for Physical Sciences at the Microscale, CAS Key Laboratory of Soft Matter Chemistry, Collaborative Innovation Center of Suzhou Nano Science and Technology, Department of Chemistry, University of Science and Technology of China
Hefei, Anhui 230026 (P. R. China)
E-mail: jianglab@ustc.edu.cn
Homepage: http://staff.ustc.edu.cn/~jianglab/
G. Wan[+]
Materials Science Division, Advanced Photon Source
Argonne National Laboratory
Lemont, IL 60439 (USA)
and
University of Chinese Academy of Sciences
Beijing, 100049 (P. R. China)
G. Wan,[+] Dr. H. Zhou
X-ray Science Division, Advanced Photon Source
Argonne National Laboratory
Lemont, IL 60439 (USA)
[+] These authors contributed equally to this work.
Supporting information and the ORCID identification number(s) for the author(s) of this article can be found under: https://doi.org/10.1002/anie.201803262.

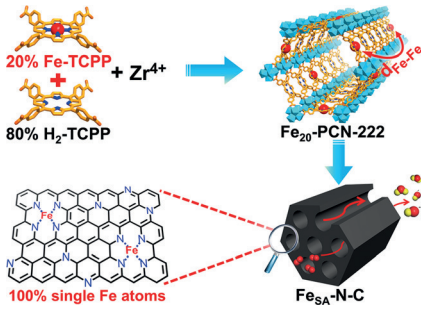

Scheme 1. Illustration of the rational fabrication of single Fe atoms-involved Fe_{SA}-N-C catalyst via a mixed-ligand strategy.

non-noble-metal catalysts and the state-of-the-art Pt/C, under both alkaline and acidic conditions.

A series of Fe_x-PCN-222, including Fe_0-PCN-222, Fe_{20}-PCN-222, and Fe_{40}-PCN-222, have been prepared and all present similarly high surface areas with uniform pore size distribution (Supporting Information, Figures S1, S2). Taking Fe_{20}-PCN-222 as a representative, its typical type-IV N_2 isotherms suggest a Brunauer–Emmett–Teller (BET) surface area as high as 2062 $m^2 g^{-1}$ and two types of pores, with sizes of 1.2 nm and 3.2 nm, corresponding to the triangular micro-channels and hexagonal mesochannels, respectively. SEM and TEM images present a uniform rod-shaped morphology with a diameter of about 200 nm (Figure 1 a; Supporting Information, Figure S3a). The highly oriented mesopores with a size of about 3.2 nm along the *c*-axis can be well identified in the TEM image (Figure 1 a, inset), in good agreement with the size distribution analysis above (Supporting Information, Figure S2). Upon pyrolysis at 800 °C, an Fe_{SA}-N-C/ZrO_2 composite with two ZrO_2 phases has been obtained (Supporting Information, Figure S4). Upon subsequent ZrO_2 removal, Fe_{20}-PCN-222 can be finally converted into Fe_{SA}-N-C without any identifiable metallic particles, and the rod shape and highly oriented mesopores in Fe_{20}-PCN-222 are inherited in the resultant Fe_{SA}-N-C to a large extent (Figure 1 b–e). N_2 sorption for Fe_{SA}-N-C suggests its high BET surface area of 532 $m^2 g^{-1}$ and the evident hysteresis loop (P/P_0: 0.6–0.8) indicates its mesoporous structure (Supporting Information, Figure S5a), which is recognizable in the cross-section SEM and TEM images (Figure 1 c–e; Supporting Information, Figure S3b). The pore size distribution analysis further manifests its hierarchical pores in 1–2 nm and about 9 nm diameters (Supporting Information, Figure S5b). It is generally believed that micropores would increase the density of active sites and mesopores are beneficial to the mass transfer, thus improving catalytic activity.[5d,9b]

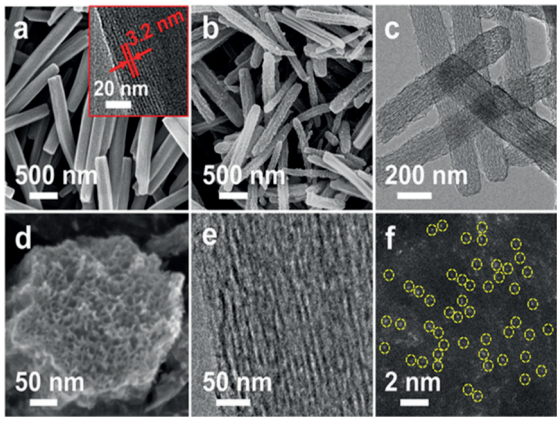

Figure 1. a) Scanning electron microscopy (SEM) image of Fe_{20}-PCN-222 (inset: transmission electron microscopy (TEM) image showing the mesochannels in Fe_{20}-PCN-222). b) SEM and c) TEM images of Fe_{SA}-N-C. d) Cross-section SEM, e) enlarged TEM images of the mesoporous structure, and f) aberration-corrected high-angle annular darkfield scanning transmission electron microscope (HAADF-STEM) images of Fe_{SA}-N-C.

The powder X-ray diffraction (PXRD) pattern of Fe_{SA}-N-C presents two broad diffraction peaks in the ranges of 20–30° and 40–45°, corresponding respectively to the (002) and (101) reflections of graphitized carbon, and no peak associated with iron-based species can be detected (Supporting Information, Figure S6). The Raman scattering spectrum for Fe_{SA}-N-C gives low intensity ratio ($I_D/I_G = 0.95$) of D band (ca. 1345 cm^{-1}) and G band (ca. 1590 cm^{-1}), further indicating its high graphitization degree, which favors electron transfer (Supporting Information, Figure S7). X-ray photoelectron spectroscopy (XPS) results reveal that C, N, O, and Fe elements are included in Fe_{SA}-N-C (Supporting Information, Figure S8a). High-resolution N 1s spectrum can be fitted into five characteristic peaks, pyridinic N (398.5 eV), Fe-N_x (399.2 eV), pyrrolic N (400.3 eV), graphitic N (401.2 eV), and oxidized N (402.7 eV), in which the Fe-N_x peak suggests the good inheritance of Fe-N_x units from Fe-TCPP after pyrolysis (Figure 2 a). The high-resolution Fe 2p spectrum with two relatively weak peaks centered at 710.7 eV (Fe $2p_{3/2}$) and 723.1 eV (Fe$2p_{1/2}$) illustrates partially oxidized Fe species in Fe_{SA}-N-C, further supporting the existence of Fe-N_x species (Supporting Information, Figure S8b).[8c] The existence of abundant N (4.67 wt %) and high loading of Fe (up to 1.76 wt %), strikingly consistent with XPS results, have been

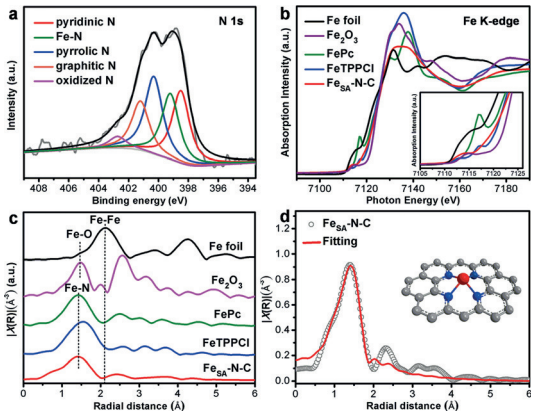

Figure 2. a) High-resolution XPS spectrum of N 1s for Fe_{SA}-N-C. b) Fe K-edge X-ray absorption near-edge structure (XANES) and c) Fourier transform-extended X-ray absorption fine structure (FT-EXAFS) spectra of Fe_{SA}-N-C, 5,10,15,20-tetraphenylporphineiron(III) chloride (FeTPPCl), and iron phthalocyanine (FePc), Fe_2O_3, and Fe foil. d) EXAFS fitting for Fe_{SA}-N-C (inset: model of Fe_{SA}-N-C. Fe red, N blue, C gray spheres).

quantified by elemental analysis and inductively coupled plasma atomic emission spectrometry (ICP-AES; Supporting Information, Table S1, S2). Aberration-corrected HAADF-STEM observation unambiguously identifies single Fe atoms from the bright spots in randomly selected areas, but no Fe particles are found (Figure 1 f; Supporting Information, Figure S9).

In addition to the localized microstructrual information above, X-ray absorption spectroscopy (XAS) was further used to unveil the electronic and structural information of Fe-involved species in Fe_{SA}-N-C. From the Fe K-edge XANES spectra, the energy absorption threshold of Fe_{SA}-N-C locates between Fe foil and Fe_2O_3 and is closer to that of FeTPPCl and FePc, implying the positively charged $Fe^{\delta+}$ stabilized by N atoms in Fe_{SA}-N-C (Figure 2 b). Furthermore, the absence of the edge peak at about 7117.1 eV, which is the fingerprint of D_{4h} symmetry, suggests the lower symmetry of Fe-N_x sites in Fe_{SA}-N-C.[3b] FT-EXAFS spectrum of Fe_{SA}-N-C at Fe K-edge presents only a main peak at about 1.44 Å, which is attributed to the Fe-N scattering path, and no Fe-Fe bond at about 2.13 Å can be detected, manifesting that the evolution of single-atom Fe sites in Fe_{SA}-N-C (Figure 2 c). To further verify the coordination structure around Fe centers, EXAFS fitting has been performed (Figure 2 d; Supporting Information, Figure S10, Table S3). The best fitting result for the first shell shows that each Fe atom is coordinated by about 4 N atoms in average, illustrating that all atomic Fe sites are four-coordinated by nitrogen species (Figure 2 d, inset). It is noteworthy that when the molar percentage of Fe-TCPP increases to 40 % in PCN-222, Fe-Fe peak is identifiable in the resultant catalyst (denoted as Fe_{NP}-N-C), manifesting that Fe atoms might aggregate to nanoparticles (NPs) upon pyrolysis with a higher percentage of Fe-TCPP, in consistent with high-resolution TEM observation results (Supporting Information, Figure S11).

The above results confirm that Fe_{20}-PCN-222 might possess an appropriate Fe-TCPP content (20 mol %) to prepare single Fe atoms. The fabrication mechanism for single Fe atoms and Fe NPs has been proposed (Supporting Information, Scheme S3). First, the mixed ligands of H_2-TCPP and Fe-TCPP (Fe is coordinated by N atoms) are employed to construct PCN-222. Its 3D skeleton composed of metal nodes and organic ligands creates the average distance (d) of adjacent Fe-TCPP ligands by simply changing the ratio of the mixed ligands. When the distance reaches to a critical value (for example, in Fe_{20}-PCN-222), the formation of Fe NPs is effectively inhibited in pyrolysis process. Upon the ZrO_2 removal, single Fe atoms anchored N-doped carbon can be successfully obtained (Supporting Information, Scheme S3b). Conversely, when more Fe-TCPP is loaded and Fe···Fe distance is shortened, Fe aggregation would be inevitable during the MOF pyrolysis (Supporting Information, Scheme S3c).

In view of the intrinsic activity of Fe-N_4 sites for efficient oxygen reduction reaction (ORR),[3,5e,11] the performance of Fe_{SA}-N-C was first investigated in 0.1 M KOH. The CV curve of Fe_0-N-C sample (obtained from Fe_0-PCN-222) without Fe doping displays a much lower oxygen reduction peak than that of Fe_{SA}-N-C and Fe_{NP}-N-C, reflecting an indispensable role of Fe-N sites on boosting ORR activity (Supporting Information, Figure S12). Linear sweep voltammetry (LSV) curves indicate the best performance of Fe_{SA}-N-C among all related catalysts, featuring a higher half-wave potential ($E_{1/2}$ = 0.891 V) than Fe_0-N-C (0.795 V), Fe_{NP}-N-C (0.889 V), and the commercial Pt/C (0.848 V) (Figure 3 a,b). Furthermore, the

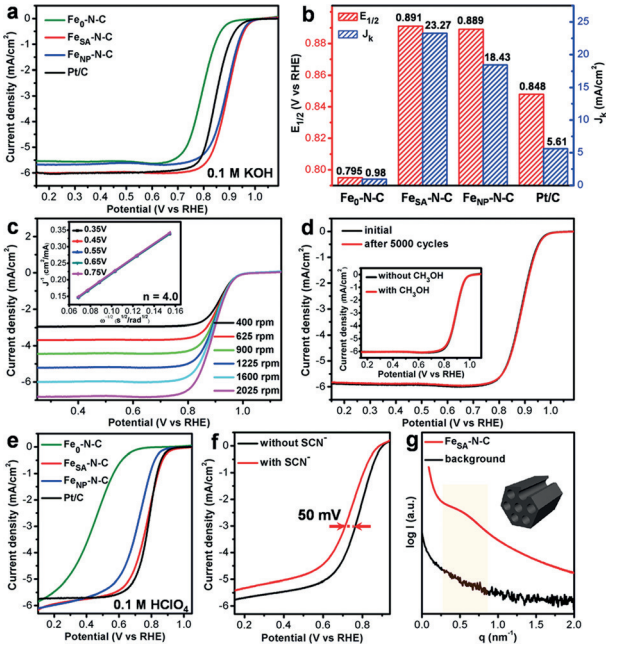

Figure 3. a) LSV curves and b) $E_{1/2}$ and J_k at 0.85 V for various catalysts in 0.1 M KOH. c) LSV curves of Fe_{SA}-N-C at different rotating rates in 0.1 M KOH (inset: K-L plots and electron transfer number). d) Stability test of Fe_{SA}-N-C (inset: methanol tolerance test) in 0.1 M KOH. e) LSV curves of various catalysts in 0.1 M $HClO_4$. f) LSV curves of Fe_{SA}-N-C in 0.1 M $HClO_4$ before and after the addition of SCN^-. g) SAXS pattern of Fe_{SA}-N-C.

superb activity of Fe_{SA}-N-C is supported by the much higher kinetic current density (J_k) at 0.85 V (23.27 mA cm^{-2}) than that of Fe_0-N-C (0.98 mA cm^{-2}), Fe_{NP}-N-C (18.43 mA cm^{-2}) and Pt/C (5.61 mA cm^{-2}), signifying its much more favorable kinetics (Figure 3 b). The LSV curve of Fe_{SA}-N-C/ZrO_2 was also obtained and its inferior performance to Fe_{SA}-N-C illustrates the importance of HF etching (Supporting Information, Figure S13). Furthermore, Fe_{SA}-N-C also shows better activity than mix-Fe-N-C, which is derived from the physical mixture of Fe-TCPP and H_2-TCPP, further demonstrating the superiority of MOFs as precursors (Supporting Information, Figure S13). All of the above results suggest that Fe_{SA}-N-C possesses the optimal activity.

To gain more insight into the electron-transfer mechanism of Fe_{SA}-N-C, LSV curves at different rotating rates of rotating disk electrode (RDE) were recorded (Figure 3 c). The K-L plots obtained from the LSV curves exhibit excellent linearity, presenting the first-order reaction kinetics for ORR with a potential-independent electron transfer rate (Figure 3 c, inset). Based on the K-L equation, the electron transfer number is determined to be about 4.0, manifesting an ideal 4 e^- ORR mechanism. Rotating ring disk electrode (RRDE)

measurement for Fe_{SA}-N-C was further performed to show the very low (< 5.5 %) H_2O_2 yields with an electron transfer number larger than 3.9 (Supporting Information, Figure S14), similar to the results from the K-L plots. Furthermore, the negligible decay of activity after stability tests and the methanol addition experiments for Fe_{SA}-N-C demonstrate its excellent durability and strong tolerance against methanol-crossover effect, in stark contrast to the significant decline of Pt/C (Figure 3 d; Supporting Information, Figure S15). The results suggest that Fe_{SA}-N-C possesses the best ORR performance among all non-noble metal catalysts ever reported under alkaline condition (Figure 3 a–d; Supporting Information, Table S4).

The excellent ORR performance of Fe_{SA}-N-C in alkaline media prompted our further exploration under the more challenging acidic condition. Strikingly, superior ORR activity with a $E_{1/2}$ of 0.776 V in 0.1 M $HClO_4$ can be achieved for Fe_{SA}-N-C, which is much higher than that of Fe_0-N-C, Fe_{NP}-N-C, Fe_{SA}-N-C/ZrO_2, mix-Fe-N-C and even comparable to (5 mV lower) that of benchmark Pt/C (Figure 3 e; Supporting Information, Figures S16, S17). The high kinetic current density (9.60 mA cm^{-2}) at 0.75 V manifests the favorable kinetics of Fe_{SA}-N-C (Supporting Information, Figure S16b). Further RRDE test suggests a H_2O_2 yield lower than 1.0 % with an ideal 4 e^- transfer process, in consistence with the result from K-L plots (Supporting Information, Figure S18). Moreover, Fe_{SA}-N-C exhibits excellent durability with only 6 mV decay after 5000 cycles and 4 % drop after the i-t test, which is much better than for Pt/C, which is possibly due to the strong affinity between atomic Fe sites and coordination N within carbon (Supporting Information, Figure S19a,c,e). Additionally, Fe_{SA}-N-C demonstrates a superior tolerance to the crossover effect of methanol compared with Pt/C, making it a promising candidate for direct application in methanol fuel cells (Supporting Information, Figure S19b,d,f). Furthermore, a preliminary constant-current test for Fe_{SA}-N-C was conducted in real fuel cell device (Supporting Information, Figure S20). It is noteworthy that, although much endeavor has been devoted, a very limited number of catalysts were reported simultaneously possessing comparable performance with Pt/C in both alkaline and acidic media, further highlighting the conspicuous advantage of the single Fe atom-involved Fe_{SA}-N-C over other reported catalysts (Supporting Information, Table S5).

To understand the origin of the excellent ORR performance of Fe_{SA}-N-C, more investigations were carried out. The SCN^- (0.01 M), with strong affinity to Fe ion, was employed as a probe to poison Fe-N_4 sites.[9c] As a result, the half-wave potential of Fe_{SA}-N-C for ORR in 0.1 M $HClO_4$ decreased significantly by 50 mV (Figure 3 f). The SCN^--poisoned electrode was subsequently rinsed with pure water and re-measured in 0.1 M KOH. The $E_{1/2}$ of the first LSV curve negatively shifts by 10 mV as compared to the original catalyst. With increasing cycle numbers, the LSV curves gradually overlap with the original one obtained before SCN^- treatment, which should be ascribed to the desorption of SCN^- from Fe site in 0.1 M KOH (Supporting Information, Figure S21). The activity recovery accompanied by the release of SCN^- from blocked Fe-N_4 sites clearly reflects that single Fe atoms are responsible for the high ORR activity of Fe_{SA}-N-C.

Furthermore, the hierarchically porous structure in Fe_{SA}-N-C is generally believed to affect the accessibility of active sites and mass transfer in catalytic process. Small-angle X-ray scattering (SAXS) for Fe_{SA}-C-N gives a broad hump between 0.28 to 0.84 nm^{-1}, hinting the ordering of pore structure with size distribution from 7 to 22 nm (Figure 3 g), in good agreement with the above microstructure observation and N_2 sorption data (Figure 1 d,e; Supporting Information, Figure S5). It should be pointed out that although reported MOF-derived carbon materials exhibit high surface areas, their pore structures are usually disordered and non-interconnected after uncontrollable pyrolysis, which is not favorable to mass transfer in catalysis.[7e,8e] Therefore, the development of porous carbon with oriented channels, which remains to be a long-term target yet a great challenge to date, has been achieved for the first time. The hierarchically porous Fe_{SA}-N-C, possessing abundant micropores (accommodating high-density Fe-N_4 active sites) and open mesoporous channels with particular orientation (facilitating the high-flux mass transfer), would greatly accelerate the ORR process (Supporting Information, Figure S22). This is in sharp contrast to sluggish mass transfer in traditional MOF-derived carbons with non-interconnected pores. Taking jointly the above Fe-N_4 active sites and pore structure merits, we may come to the conclusion that single-atom Fe sites accessible by hierarchal pores in Fe_{SA}-N-C mainly contribute to the superb ORR performance.

In summary, we have developed a novel mixed-ligand strategy in MOF system to fabricate SACs. The ratio optimization of the mixed porphyrin ligands with and without Fe^{III} centers gives rise to long spatial distance of Fe^{III} ions in the MOF skeleton, favoring the formation of single Fe atoms upon pyrolysis. Benefiting from periodic and tailorable MOF structures, the spatial distance control of Fe^{III} in porphyrinic MOFs effectively suppresses the Fe aggregation during pyrolysis, leading to atomic dispersion of Fe with a high loading (1.76 wt %) in porous carbon. Thanks to the single-atom Fe sites (superior activity), hierarchically porous structure (accessible active sites) with oriented mesopores (fast diffusion of O_2 and electrolyte), and high conductivity (fast electron transfer), Fe_{SA}-N-C demonstrates excellent ORR performance in both alkaline and acidic media, surpassing any other reported non-noble-metal catalysts and even the Pt/C. In light of the tremendous diversity and tailorability of MOFs, this work opens up an avenue to the rational synthesis of efficient SACs via multiscale control.

Acknowledgements

This work is supported by the NSFC (21725101, 21673213 and 21521001), the 973 program (2014CB931803), the Fundamental Research Funds for the Central Universities (WK2060030029), and the Recruitment Program of Global Youth Experts. Use of the Advanced Photon Source is supported by the U.S. Department of Energy, Office of Science, Office of Basic Energy Sciences, under Contract No.

DE-AC02-06CH11357. We are grateful to the reviewers for valuable suggestions, and Dr. Chenxi Xu at Hefei Univ. Technol. for great help on the testing of the fuel cell device.

Conflict of interest

The authors declare no conflict of interest.

Keywords: metal–organic frameworks · oxygen reduction reaction · porous carbon · single-atom catalysts

How to cite: *Angew. Chem. Int. Ed.* **2018**, *57*, 8525 – 8529
Angew. Chem. **2018**, *130*, 8661 – 8665

[1] a) C. Zhu, S. Fu, Q. Shi, D. Du, Y. Lin, *Angew. Chem. Int. Ed.* **2017**, *56*, 13944 – 13960; *Angew. Chem.* **2017**, *129*, 14132 – 14148; b) H. Zhang, G. Liu, L. Shi, J. Ye, *Adv. Energy Mater.* **2018**, *8*, 1701343; c) Z. Zhang, Y. Zhu, H. Asakura, B. Zhang, J. Zhang, M. Zhou, Y. Han, T. Tanaka, A. Wang, T. Zhang, N. Yan, *Nat. Commun.* **2017**, *8*, 16100; d) Y. Zheng, Y. Jiao, Y. Zhu, Q. Cai, A. Vasileff, L. H. Li, Y. Han, Y. Chen, S. Z. Qiao, *J. Am. Chem. Soc.* **2017**, *139*, 3336 – 3339.

[2] a) B. Qiao, A. Wang, X. Yang, L. F. Allard, Z. Jiang, Y. Cui, J. Liu, J. Li, T. Zhang, *Nat. Chem.* **2011**, *3*, 634 – 641; b) J. Liu, *ACS Catal.* **2017**, *7*, 34 – 59; c) L. Fan, P. F. Liu, X. Yan, L. Gu, Z. Z. Yang, H. G. Yang, S. Qiu, X. Yao, *Nat. Commun.* **2016**, *7*, 10667.

[3] a) Y. J. Sa, D.-J. Seo, J. Woo, J. T. Lim, J. Y. Cheon, S. Y. Yang, J. M. Lee, D. Kang, T. J. Shin, H. S. Shin, H. Y. Jeong, C. S. Kim, M. G. Kim, T.-Y. Kim, S. H. Joo, *J. Am. Chem. Soc.* **2016**, *138*, 15046 – 15056; b) A. Zitolo, V. Goellner, V. Armel, M.-T. Sougrati, T. Mineva, L. Stievano, E. Fonda, F. Jaouen, *Nat. Mater.* **2015**, *14*, 937 – 942.

[4] a) P. Liu, Y. Zhao, R. Qin, S. Mo, G. Chen, L. Gu, D. M. Chevrier, P. Zhang, Q. Guo, D. Zang, B. Wu, G. Fu, N. Zheng, *Science* **2016**, *352*, 797 – 800; b) P. Yin, T. Yao, Y. Wu, L. Zheng, Y. Lin, W. Liu, H. Ju, J. Zhu, X. Hong, Z. Deng, G. Zhou, S. Wei, Y. Li, *Angew. Chem. Int. Ed.* **2016**, *55*, 10800 – 10805; *Angew. Chem.* **2016**, *128*, 10958 – 10963.

[5] a) L. Jiao, Y.-X. Zhou, H.-L. Jiang, *Chem. Sci.* **2016**, *7*, 1690 – 1695; b) H. Fei, J. Dong, M. J. Arellano-Jiménez, G. Ye, N. D. Kim, E. L. G. Samuel, Z. Peng, Z. Zhu, F. Qin, J. Bao, M. J. Yacaman, P. M. Ajayan, D. Chen, J. M. Tour, *Nat. Commun.* **2015**, *6*, 8668; c) H. W. Liang, X. Zhuang, S. Bruller, X. Feng, K. Müllen, *Nat. Commun.* **2014**, *5*, 4973; d) Z. Qian, Z. Hu, Z. Zhang, Z. Li, M. Dou, F. Wang, *Catal. Sci. Technol.* **2017**, *7*, 4017 – 4023; e) M. Lefèvre, E. Proietti, F. Jaouen, J.-P. Dodelet, *Science* **2009**, *324*, 71 – 74; f) J. Zhang, L. Dai, *ACS Catal.* **2015**, *5*, 7244 – 7253.

[6] a) H.-C. Zhou, J. R. Long, O. M. Yaghi, *Chem. Rev.* **2012**, *112*, 673 – 674; b) H.-C. Zhou, S. Kitagawa, *Chem. Soc. Rev.* **2014**, *43*, 5415 – 5418; c) T. Islamoglu, S. Goswami, Z. Li, A. J. Howarth, O. K. Farha, J. T. Hupp, *Acc. Chem. Res.* **2017**, *50*, 805 – 813; d) B. Li, H.-M. Wen, Y. Cui, W. Zhou, G. Qian, B. Chen, *Adv. Mater.* **2016**, *28*, 8819 – 8860; e) L. Jiao, Y. Wang, H.-L. Jiang, Q. Xu, *Adv. Mater.* **2018**, https://doi.org/10.1002/adma.201703663; f) M. Zhao, K. Yuan, Y. Wang, G. Li, J. Guo, L. Gu, W. Hu, H. Zhao, Z. Tang, *Nature* **2016**, *539*, 76 – 80.

[7] a) B. Liu, H. Shioyama, T. Akita, Q. Xu, *J. Am. Chem. Soc.* **2008**, *130*, 5390 – 5391; b) S. Ma, G. A. Goenaga, A. V. Call, D.-J. Liu, *Chem. Eur. J.* **2011**, *17*, 2063 – 2067; c) B. Y. Xia, Y. Yan, N. Li, H. B. Wu, X. W. Lou, X. Wang, *Nat. Energy* **2016**, *1*, 15006; d) Y.-Z. Chen, C. Wang, Z.-Y. Wu, Y. Xiong, Q. Xu, S.-H. Yu, H.-L. Jiang, *Adv. Mater.* **2015**, *27*, 5010 – 5016; e) K. Shen, X. Chen, J. Chen, Y. Li, *ACS Catal.* **2016**, *6*, 5887 – 5903; f) H. Zhang, S. Hwang, M. Wang, Z. Feng, S. Karakalos, L. Luo, Z. Qiao, X. Xie, C. Wang, D. Su, Y. Shao, G. Wu, *J. Am. Chem. Soc.* **2017**, *139*, 14143 – 14149; g) Q. Lin, X. Bu, A. Kong, C. Mao, X. Zhao, F. Bu, P. Feng, *J. Am. Chem. Soc.* **2015**, *137*, 2235 – 2238; h) Z. Zhu, Y. Yang, Y. Guan, J. Xue, L. Cui, *J. Mater. Chem. A* **2016**, *4*, 15536 – 15545.

[8] a) Y. V. Kaneti, J. Tang, R. R. Salunkhe, X. Jiang, A. Yu, C.-W. Wu, Y. Yamauchi, *Adv. Mater.* **2017**, *29*, 1604898; b) F. Meng, H. Zhong, D. Bao, J. Yan, X. Zhang, *J. Am. Chem. Soc.* **2016**, *138*, 10226 – 10231; c) Y. Ye, F. Cai, H. Li, H. Wu, G. Wang, Y. Li, S. Miao, S. Xie, R. Si, J. Wang, X. Bao, *Nano Energy* **2017**, *38*, 281 – 289; d) Y. Qian, I. A. Khan, D. Zhao, *Small* **2017**, *13*, 1701143; e) W. Xia, R. Zou, L. An, D. Xia, S. Guo, *Energy Environ. Sci.* **2015**, *8*, 568 – 576; f) K. J. Lee, J. H. Lee, S. Jeoung, H. R. Moon, *Acc. Chem. Res.* **2017**, *50*, 2684 – 2692; g) H. B. Wu, X. W. Lou, *Sci. Adv.* **2017**, *3*, eaap9252.

[9] a) Q. Lai, L. Zheng, Y. Liang, J. He, J. Zhao, J. Chen, *ACS Catal.* **2017**, *7*, 1655 – 1663; b) X. Sun, A. I. Olivos-Suarez, D. Osadchii, M. J. V. Romero, F. Kapteijn, J. Gascon, *J. Catal.* **2018**, *357*, 20 – 28; c) Y. Chen, S. Ji, Y. Wang, J. Dong, W. Chen, Z. Li, R. Shen, L. Zheng, Z. Zhuang, D. Wang, Y. Li, *Angew. Chem. Int. Ed.* **2017**, *56*, 6937 – 6941; *Angew. Chem.* **2017**, *129*, 7041 – 7045.

[10] a) D. Feng, Z.-Y. Gu, J.-R. Li, H.-L. Jiang, Z. Wei, H.-C. Zhou, *Angew. Chem. Int. Ed.* **2012**, *51*, 10307 – 10310; *Angew. Chem.* **2012**, *124*, 10453 – 10456; b) W. Morris, B. Volosskiy, S. Demir, F. Gándara, P. L. McGrier, H. Furukawa, D. Cascio, J. F. Stoddart, O. M. Yaghi, *Inorg. Chem.* **2012**, *51*, 6443 – 6445; c) Y. Chen, T. Hoang, S. Ma, *Inorg. Chem.* **2012**, *51*, 12600 – 12602.

[11] a) L. Cui, G. Lv, X. He, *J. Power Sources* **2015**, *282*, 9 – 18; b) S. Gupta, D. Tryk, I. Bae, W. Aldred, E. Yeager, *J. Appl. Electrochem.* **1989**, *19*, 19 – 27; c) C. W. B. Bezerra, L. Zhang, K. Lee, H. Liu, A. L. B. Marques, E. P. Marques, H. Wang, J. Zhang, *Electrochim. Acta* **2008**, *53*, 4937 – 4951; d) M. Zhou, H.-L. Wang, S. Guo, *Chem. Soc. Rev.* **2016**, *45*, 1273 – 1307; e) J.-C. Li, Z.-Q. Yang, D.-M. Tang, L. Zhang, P.-X. Hou, S.-Y. Zhao, C. Liu, M. Cheng, G.-X. Li, F. Zhang, H.-M. Cheng, *NPG Asia Mater.* **2018**, *10*, e461.

Manuscript received: March 17, 2018
Revised manuscript received: April 29, 2018
Accepted manuscript online: May 9, 2018
Version of record online: June 12, 2018

